PAPER

Janus bottlebrush compatibilizers†‡

Zhan Chen, [ID] §[a] Hong-Gyu Seong, [ID] §[a] Mingqiu Hu, [ID] [a] Xuchen Gan, [ID] [a] Alexander E. Ribbe, [ID] [a] Jaechul Ju,[b] Hanyu Wang,[c] Mathieu Doucet, [ID] [d] Todd Emrick [ID] *[a] and Thomas P. Russell [ID] *[ae]

Bottlebrush random copolymers (BRCPs), consisting of a random distribution of two homopolymer chains along a backbone, can segregate to the interface between two immiscible homopolymers. BRCPs undergo a reconfiguration, where each block segregates to one of the homopolymer phases, adopting a Janus-type structure, reducing the interfacial tension and promoting adhesion between the two homopolymers, thereby serving as a Janus bottlebrush copolymer (JBCP) compatibilizer. We synthesized a series of JBCPs by copolymerizing deuterated or hydrogenated polystyrene (DPS/PS) and poly(*tert*-butyl acrylate) (PtBA) macromonomers using ruthenium benzylidene-initiated ring-opening metathesis polymerization (ROMP). Subsequent acid-catalyzed hydrolysis converted the PtBA brushes to poly(acrylic acid) (PAA). The JBCPs were then placed at the interface between DPS/PS homopolymers and poly(2-vinyl pyridine) (P2VP) homopolymers, where the degree of polymerization of the backbone (N_{BB}) and the grafting density (GD) of the JBCPs were varied. Neutron reflectivity (NR) was used to determine the interfacial width and segmental density distributions (including PS homopolymer, PS block, PAA block and P2VP homopolymer) across the polymer-polymer interface. Our findings indicate that the star-like JBCP with $N_{BB} = 6$ produces the largest interfacial broadening. Increasing N_{BB} to 100 (rod-like shape) and 250 (worm-like shape) reduced the interfacial broadening due to a decrease in the interactions between blocks and homopolymers by stretching of blocks. Decreasing the GD from 100% to 80% at $N_{BB} = 100$ caused an increase the interfacial width, yet further decreasing the GD to 50% and 20% reduced the interfacial width, as 80% of GD may efficiently increase the flexibility of blocks and promote interactions between homopolymers, while maintaining relatively high number of blocks attached to one molecule. The interfacial conformation of JBCPs was further translated into compatibilization efficiency. Thin film morphology studies showed that only the lower N_{BB} values ($N_{BB} = 6$ and $N_{BB} = 24$) and the 80% GD of $N_{BB} = 100$ had bicontinuous morphologies, due to a sufficient binding energy that arrested phase separation, supported by mechanical testing using asymmetric double cantilever beam (ADCB) tests. These provide fundamental insights into the assembly behavior of JBCPs compatibilizers at homopolymer interfaces, opening strategies for the design of new BCP compatibilizers.

[a] *Department of Polymer Science and Engineering, University of Massachusetts Amherst, Amherst, MA, 01003, USA. E-mail: tom.p.russell@gmail.com*

[b] *Department of Chemistry, The University of Texas at Austin, Austin, TX, 78712, USA*

[c] *Center for Nanophase Materials Sciences, Oak Ridge National Laboratory, Oak Ridge, TN, 37831, USA*

[d] *Neutron Scattering Division, Oak Ridge National Laboratory, Oak Ridge, TN, 37831, USA*

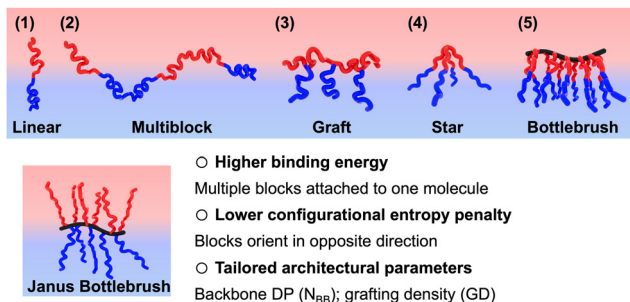[e] *Materials Sciences Division, Lawrence Berkeley National Laboratory, Berkeley, CA, 37831, USA*

† Electronic supplementary information (ESI) available. See DOI: https://doi.org/10.1039/d3sm01484c

‡ Zu Ehren von Professor Doktor Ullrich Steiner anlässlich seines sechzigsten Geburtstages. Lieber Ulli, nur sechzig, trotzdem einer Junger! Schaeffst Du mehr und hast Du Spass! (In honor of Professor Doctor Ullrich Steiner on the occasion of his sixtieth birthday. Dear Ulli, only sixty, but still a young one! Do more and have fun!).

§ Zhan Chen and Hong-Gyu Seong contributed equally to this work.

Introduction

The surge in global plastic production underscores an urgency to devise more efficient strategies for polymer recycling and upcycling.[1] Most recycling is mechanical, where multiple plastics are masticated in an extruder to yield a composite.[2,3] However, the inherent immiscibility of polymers leads to macroscopic phase-separation and narrow interfacial widths between the dissimilar polymers,[3] making the composite susceptible to mechanical failure at the interfaces.[4] With block copolymer (BCP) compatibilizers,[3] where each block is miscible with one component of the blend, the segregation of the BCP to the interface decreases interfacial energies with reduced size of the homopolymer domains, and effectively stitch the homopolymer domains, promoting adhesion between the dissimilar polymers.[5,6]

Scheme 1 Block copolymers (BCPs) as macromolecular compatibilizers.

Recent advances in BCP compatibilizers leverage polymer architecture for enhanced performance, primarily aiming to increase binding energy of the molecules to the interface.[5] For instance, as shown in Scheme 1, linear multiblock copolymers showed superior adhesion in comparison to their diblock counterparts, due to the multiple anchoring points to the interface.[7] Similarly, for graft polymers, where the backbone of the polymer chain weaves across the interface, a greater compatibilization efficiency is found due to improved stress transfer between the phases.[8–10] Another category within advanced architectural BCPs is derived from combining multiple linear BCPs at a central point or sequentially along linear backbone, forming star or bottlebrush BCPs.[11,12] These architectures having multiple BCP chains per molecule can further enhance the binding energy per molecule.

While the varied polymer architectures promise higher binding energies per polymer chain, they may also introduce a configurational entropic penalty, that may limit their utility as compatibilizers or adhesion promoters. Therefore, understanding the equilibrium conformation of these advanced architectural BCPs is important. Experimentally, neutron reflectivity,[13,14] dynamic secondary ion mass spectroscopy,[15,16] and forward recoil spectroscopy[17,18] can be used to quantify the segment density distribution of polymers at interfaces, thereby elucidating their configuration. For example, linear diblock copolymers adopt an average normal orientation to an interface, optimizing enthalpic interactions,[19] whereas multiblock copolymers are more parallelly aligned with the interface.[6,15] For graft copolymers of the same block length, the location of the branched block can profoundly influence interfacial tension, due to varying configurations at interface. Mid-grafted architectures showed the lowest interfacial tension when compared to double-end-grafted, single-end grafted, and even-grafted architectures.[9] For star BCPs, the core and corona blocks are under different constraints and adopt different configurations, with core blocks under greater compression near the interface.[14] It was found that the arms of star BCPs tilt at both fluid–fluid and homopolymer–homopolymer interfaces. The tilt angle increases with number of arms, as evidenced by the larger radius of gyration at the interface.[20,21]

To further enhance compatibilization efficiency, there is a need to design BCP architectures that enhance the binding energy per chain without significantly reducing the configurational entropy. Compared to multiblock and star BCPs, bottlebrush BCPs effectively have a high lineal density of polymer

chains connected to a backbone, significantly increasing the binding energy per chain. There have been efforts using random bottlebrush (random copolymer linearly attached to backbone) and Janus nanoparticles (JNPs) to achieve a similar goal, which mainly focused on the macroscopic compatibilization behavior such as morphology and the mechanical properties. However, it is demanding to perform an in-depth investigation on the interfacial conformation for understanding the behind compatibilization mechanism.[22–26] In this study, bottlebrush random copolymers (BRCPs), where two homopolymer chains are randomly attached to a backbone chain, are shown to adopt a Janus-type configuration at a homopolymer interface, placing the different chains in the different phases.[27] This reconfiguration effectively reduces steric crowding at interface, with less cost of configurational entropic penalty compared to bottlebrush BCPs. In addition, the BRCP architecture offers several other advantages, including (1) an ease in characterizing the molecular weight of the side-chains; (2) a composition defined by the synthesis; (3) a well-defined backbone chain length; and (4) simple routes to control grafting density.[27–30]

In this work, we investigated symmetric BRCPs prepared by copolymerization of hydrogenated or deuterated polystyrene (PS/DPS) and poly (*tert*-butyl acrylate) (P*t*BA) macromonomers *via* ruthenium benzylidene-initiated ring-opening metathesis polymerization (ROMP). By acid-catalyzed hydrolysis, the P*t*BA blocks were converted to poly(acrylic acid) (PAA) blocks.[31] These BRCPs were placed directly at the interface between PS/ DPS homopolymer and hydrogenated or deuterated poly(2-vinyl pyridine) (P2VP/DP2VP) homopolymers.[32,33] Upon thermal annealing, the BRCPs assumed a Janus-type configuration at the interface. The DPS/PS chains and PAA chains were found to segregate to the DP/PS homopolymer and DP2VP/P2VP homopolymer, respectively, thus serving as Janus bottlebrush compatibilizers (JBCPs). The degree of polymerization of the backbone (N_{BB}) and the grafting density (GD) of the JBCPs were varied, the latter by incorporating phenyl-substituted norbornene as a spacer.[27] At a constant side chain length (N_{SC}), increasing N_{BB} stretches the side chains (blocks), transitioning the macromolecular shape from star-like to rod-like, then eventually to worm-like.[34,35] The change in N_{BB} markedly affects block configuration, the interactions between blocks and homopolymers, and the overall compatibilization efficiency (including interfacial energy and adhesion strength). Since GD determines the packing density of the blocks along the backbone, manipulating GD can alter block flexibility, subsequently influencing compatibilization efficiency. By selective deuterium labeling of the blocks or homopolymers, neutron reflectivity (NR) are used to measure the interfacial width to probe the interfacial energy.[33] Additionally, NR was also used to determine the segmental density distribution normal to interface of the PS homopolymer, PS block, PAA block and P2VP homopolymers, providing a deeper understanding of JBCP configuration at interface.[13] We further explored the structure-properties relationship by analyzing the morphology of thin films of the blend and measuring the adhesion strength of trilayer samples.[36–38]

Results and discussion

Synthesis of Janus bottlebrush compatibilizers (JBCPs)

The poly(*tert*-butyl acrylate) (NB-P*t*BA) and deuterated or hydrogenated polystyrene (NB-DPS or NB-PS) macromonomers (MMs) with norbornene ω-chain ends were synthesized by a three-step process: (1) atom-transfer radical polymerization of either *tert*-butyl acrylate or (deuterated) styrene monomers, (2) azidation of the ω-chain ends, and (3) Huisgen 1,3-dipolar cycloaddition. Detailed information regarding macromonomer synthesis and characterizations is found in the ESI.† Using these macromonomers, BRCPs containing P*t*BA and DPS/PS side chains were prepared by ring-opening metathesis polymerization (ROMP) using the Grubbs 3rd generation initiator (G3, (H$_2$IMes)(Cl)$_2$(pyr)$_2$RuCHPh) (Fig. 1a). The DP of the side chain (N_{SC}) for PS, DPS and P*t*BA was fixed as 21, 20 and 32, respectively. The DP of the backbone (N_{BB}) was adjusted by the [MMs]:[G3] ratio (Fig. 1b), varying the samples structure to include 6, 24, 100 and 250. Depending on the N_{BB} to N_{SC} ratio, the shape of bottlebrush polymer will fall into star-like ($N_{BB} \ll N_{SC}$), rod-like ($N_{BB} \approx N_{SC}$), or worm-like ($N_{BB} \gg N_{SC}$) regime.[34,35] Additionally, the grafting density (GD) of the RBCPs was controlled by inclusion of a phenyl-substituted norbornene (NB-Ph) in the copolymerization strategy with GD calculated as [MMs]/([MMs] + [NB-Ph]) (Fig. 1c).[27] The random distribution of NB-Ph was confirmed by kinetic study. The *tert*-butyl acrylates of the resulting BRCPs were subsequently hydrolyzed under acidic conditions (using trifluoroacetic acid as catalyst, TFA) to transform them into acrylic acids and yield the amphiphilic RBCPs with poly(acrylic acid) (PAA) and DPS/PS side chains.[31]
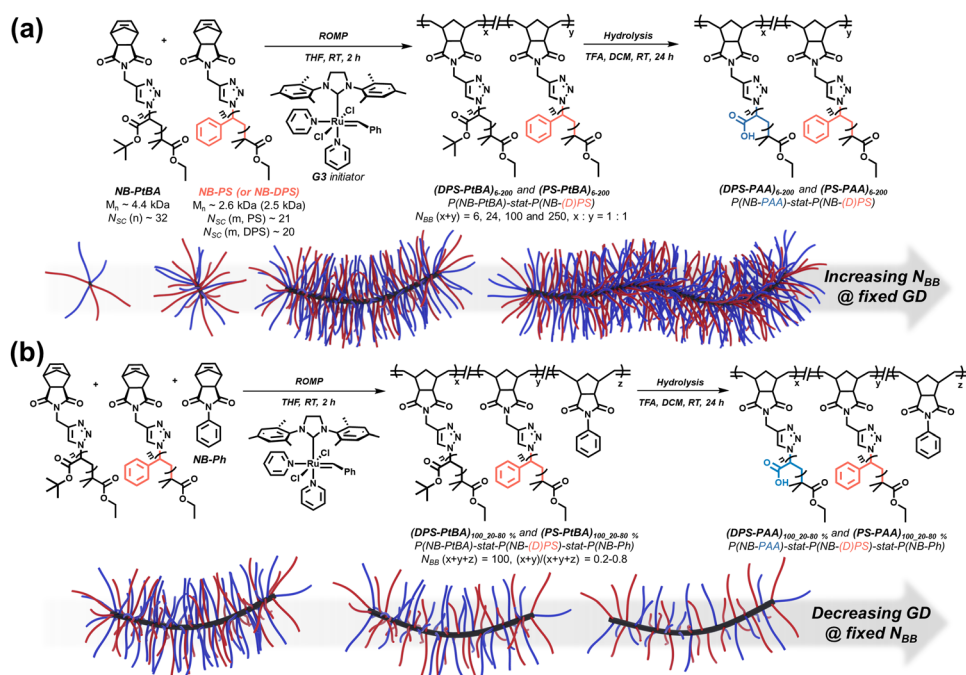
During the hydrolysis, the polymers precipitated, subjected to multiple washes with dichloromethane (DCM), then dried under vacuum to obtain the final product. Comprehensive procedures and characterization results can be found in Table 1 and ESI† (Fig. S1–S19).

In the bulk, the BRCPs before hydrolysis microphase separated into lamellar microdomains of PS and P*t*BA and, as such, the BRCP assumes a Janus-type conformation, with DPS/PS and P*t*BA side chains segregated to opposite sides of the backbone.[39,40]

Half of the domain spacing was measured to be 8.0 nm (equivalent to the molecular width) that decreased to 6.6 nm post-conversion (Fig. S20, ESI†).[41] Despite the increase of $\chi_{PS-PtBA}$ from 0.264 to 0.885 for χ_{PS-PAA}, the domain size decreased due to volume reduction of P*t*BA upon hydrolysis to PAA.[42,43] Notably, a 3rd order interference was seen after conversion, signifying enhanced phase separation and an improvement in long-range order due to increment of χ.

Interfacial width

The compatibilization efficiency is controlled by the interfacial energy between the two homopolymers, *i.e.*, a high interfacial energy produces sharper interfaces and, hence, interfacial failure and poor mechanical properties are observed. To probe composite polymer structures, neutron reflectivity (NR) measurements were performed on trilayer of (DPS-PAA)$_n$ sandwiched between DPS and P2VP on a silicon substrate, denoted DPS||(DPS-PAA)$_n$||P2VP||Si (Fig. 2a). The thickness of each layer was measured independently by ellipsometry, where DPS and P2VP layer were $\sim$80 nm and (DPS-PAA)$_n$ layer was

Fig. 1 (a) ROMP of NB-P*t*BA and NB-DPS/PS, and subsequent acid-catalyzed hydrolysis of *t*-BA repeating units. Illustrations of polymer shapes as a function of N_{BB}. (b) ROMP of NB-P*t*BA, NB-DPS/PS, and NB-Ph, and subsequent acid-catalyzed hydrolysis of *t*-BA repeating units. Illustrations of polymer shapes as a function of GD. PS is shown as example in scheme.

Table 1 Characterization data for ((D)PS–PtBA)$N_{BB\_GD\%}$

Entry	Target N_{BB} ([MMs]/[G3])	Target GD (%)	$M_{n, theo}$ (kDa)	GD[a] (%)	$M_{n, MALLS-SEC}$ (kDa)	$M_{w, MALLS-SEC}$ (kDa)	PDI
(PS-PtBA)$_6$	6	100	21	100	23.1	26.8	1.17
(PS-PtBA)$_{24}$	24	100	84	100	71.4	82.9	1.16
(PS-PtBA)$_{100}$	100	100	350	100	287.0	347.3	1.21
(PS-PtBA)$_{250}$	250	100	875	100	694.4	913.0	1.31
(PS-PtBA)$_{100\_80\%}$	100	80	284	80	234.4	289.4	1.23
(PS-PtBA)$_{100\_50\%}$	100	50	187	50	163.8	202.4	1.24
(PS-PtBA)$_{100\_20\%}$	100	20	89	20	75.1	89.2	1.19
(DPS-PtBA)$_6$	6	100	21	100	24.1	29.5	1.23
(DPS-PtBA)$_{24}$	24	100	83	100	83.7	99.4	1.19
(DPS-PtBA)$_{100}$	100	100	345	100	376.5	487.1	1.29
(DPS-PtBA)$_{250}$	250	100	862	100	869.4	1277.0	1.47
(DPS-PtBA)$_{100\_80\%}$	100	80	281	80	296.1	377.7	1.28
(DPS-PtBA)$_{100\_50\%}$	100	50	184	50	180.4	220.9	1.22
(DPS-PtBA)$_{100\_20\%}$	100	20	88	20	90.1	107.7	1.19

[a] GD was based on the feed ratio and monomer conversion as judged by disappearance of the resonance at 6.34 ppm in the ^{1}H NMR spectrum, which corresponds to the vinyl protons of the norbornene monomers. Overlap of the phenyl resonances of NB-Ph and the PS brushes preclude spectroscopic identification of NB-Ph units in the bottlebrush product.

~5 nm. In terms of neutron scattering length densities (SLD), the thermally annealed trilayers reduce to a bilayer, where DPS layer is on top of hydrogenated layer of P2VP with penetrated PAA. The difference in the SLDs of the PAA and P2VP is minimal and the contrast arises predominantly from the change in the SLD at the interface between DPS and P2VP.

As shown in Fig. 2b, all neutron reflectivity showed total external reflection at 0.018 Å^{-1}, corresponding to the critical angle between DPS layer and the air surface.[44] The Kiessig fringes in NR reflect the thickness of the DPS layer, while the decay in amplitude reflects the width of the interface with P2VP. Compared to a control sample, it is evident that adding JBCP dampens the Kiessig fringes at smaller q, due to the increased interfacial width between the DPS and P2VP layers. From the SLD profiles used to fit the NR (Fig. S21, ESI†), the interfacial width (α_I), defined as

$$\alpha_I = \frac{\Delta_{SLD}}{(dSLD/dz)_{SLD=\frac{1}{2}(DPS+P2VP)}},$$

can be determined from the concentration profiles.[33,44] Fig. 2c showed that JBCPs can efficiently increase interfacial width from 3.1 nm absent the JBCP, to 4.5 nm, 3.8 nm, 3.7 nm and 3.8 nm for N_{BB} = 6, 24, 100 and 250 respectively. For N_{BB} = 6 (the starlike JBCP), the interfacial width is broadest. Increasing N_{BB} reduces the flexibility of JBCP and introduces a configurational entropy penalty. Given the short length of the block (~30 repeating units) compared to homopolymer chain length (~2500 repeating units), the JBCPs effectively acts as a small molecule solubilizer. For larger N_{BB}, where the JBCP is rod or worm-like, penetration of the homopolymer into the brush is limited, narrowing the interfacial width. This can be mediated by decreasing the grafting density. As shown in Fig. 2d and e, reducing the GD increases the interfacial width from 3.7 nm (DPS-PtBA)$_{100}$ to 10.7 nm (DPS-PtBA)$_{100\_80\%}$, However, the interfacial width then decreases to 4.9 nm and 4.5 nm as the GD is decreased further to (DPS-PtBA)$_{100\_50\%}$ and (DPS-PtBA)$_{100\_20\%}$,

respectively, resulting from the decreased number of side chains that can interact favorably with the homopolymers. These results are consistent with our previous studies, where star-like JBCP and cylindrical-like JBCP with medium GD showed lowest interfacial tension values at the water–oil interface.[27]

Segmental density distribution

To gain comprehensive understanding of the architectural influence of JBCP for compatibilization, it is necessary to examine the segmental density distributions of both the blocks and homopolymers. We prepared trilayer samples of PS||(DPS-PAA)$_n$||DP2VP||Si, where deuterated layer and hydrogenated layer are alternated, enhancing SLD contrast at all of the interfaces (Fig. S22 and S23, ESI†). Knowing the thicknesses and position of each layer, the segment density distributions are determined for PS homopolymer, PS block, PAA block and P2VP homopolymer. By adding the segmental density distribution of the block and its corresponding homopolymer, we obtain the total segment density distribution, allowing for direct comparison to the total segmental density distribution derived from DPS ||(DPS-PAA)$_n$||P2VP||Si contrast. Fig. 3 summarizes the segmental density distributions for variable N_{BB}. For N_{BB} = 6 and 24, the PAA and PS blocks show greater miscibility than the homopolymers, as is also seen in PS||(DPS-PAA)$_n$||P2VP||Si (Fig. S24, ESI†). At first glance, this higher miscibility might seem counterintuitive, especially given a χ value of 0.885 between PS and PAA. However, since (1) JBCPs fall in the "dry brush" regime, where the two blocks are suppressed near the interface,[45–47] and (2) the covalent connection between relevant short blocks could enhance the miscibility further,[48] it is reasonable that two blocks showed greater miscibility compared to their corresponding homopolymers. Since the shape of JBCP, dependent on the N_{BB}, can range from spherical to rod-like to worm-like, such characteristic shape might facilitate in-plane ordering at the interface, a phenomenon widely documented in polymer-grafted nanoparticles at fluids interface.[49] However, the limited q range in
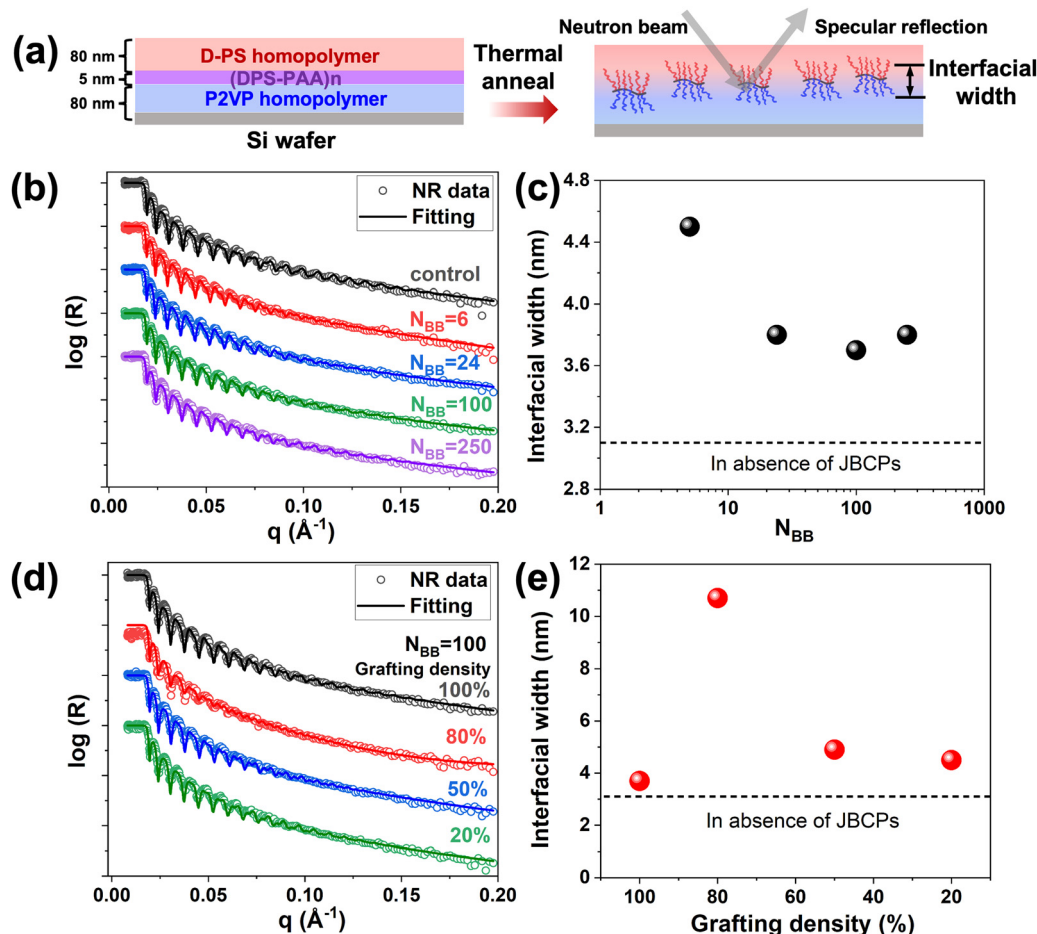
Fig. 2 (a) Schematic illustration of probing interfacial width from neutron reflectivity (NR); (b) NR of DPS||(DPS-PAA)$_n$||P2VP||Si for different N_{BB} of JBCPs. The NR profiles are shifted for clarity. (c) Interfacial width between PS and P2VP homopolymer in presence of JBCPs of variable N_{BB} at 100% GD. (d) Neutron reflectivity (NR) of DPS||(DPS-PAA)$_n$||P2VP||Si for different GD values at N_{BB} = 100. The NR profiles are shifted for clarity. (e) Interfacial width between PS and P2VP homopolymer in presence of JBCPs with variation of grafting density at N_{BB} = 100.

NR images from both PS||(DPS-PAA)$_n$||DP2VP||Si and DPS||(DPS-PAA)$_n$||P2VP||Si only predominantly yielded specular reflection (Fig. S25, ESI†). Future investigation using grazing-incidence small angle neutron scattering (GISANS) is needed to characterize the in-plane ordering.[50]

The segmental density distribution profile allows us to calculate surface excess (Γ) for each block using

$$\Gamma = \int_{-\infty}^{\infty} \Phi_{blocks} d_z.$$

The Γ for the entire JBCP molecule can be derived as

$$\Gamma_{JBCP} = \int_{-\infty}^{\infty} (\Phi_{PS\ block} + \Phi_{PAA\ block}) d_z.$$

Given the uniformity of side chains (blocks) across different architectures and consistent sample preparation conditions, Γ remains relatively constant, with average Γ value for different N_{BB} determined as 2.4 ± 0.1 nm, 2.1 ± 0.3 nm and 4.4 ± 0.5 nm for $\Gamma_{PS\ block}$, $\Gamma_{PAA\ block}$ and Γ_{JBCP}, respectively (Fig. S26, ESI†). From the segmental density distribution profiles, we can determine the interfacial width by evaluating total segment density

distributions of PS (blocks + PS homopolymers) and P2VP (PAA blocks + P2VP homopolymers). The observed trend in interfacial width (Fig. 4a) aligned with measurements from DPS||(DPS-PAA)$_n$||P2VP||Si. We calculated averaged block position using

$$z = \frac{\int_{-\infty}^{\infty} z d\Phi_{block}}{\int_{-\infty}^{\infty} d\Phi_{block}},$$

and the distance between two blocks can then be derived as $d = z_{PS\ block} - z_{PAA\ block}$, where the interface is aligned at $z = 0$ with PS position positive and PAA position negative. As shown in Fig. 4b, the distance between blocks (d) exhibits a trend with respect to N_{BB}. For N_{BB} = 6, d is 0.2 nm, which increases to 0.7 nm for N_{BB} = 24. d peaks at 4.6 nm of N_{BB} = 100, then decreases slightly to 4.2 nm of N_{BB} = 250. The trend suggests that as N_{BB} increases, the blocks stretch further due to steric hindrance caused by densely packed chains. The stretching effect reduces the interaction between the block and its corresponding homopolymers, resulting in a narrower interfacial width (Scheme 2). As N_{BB} increases, the PS block volume fraction maximum ($\phi_{PS\ maximum}$) decreases while the PAA block
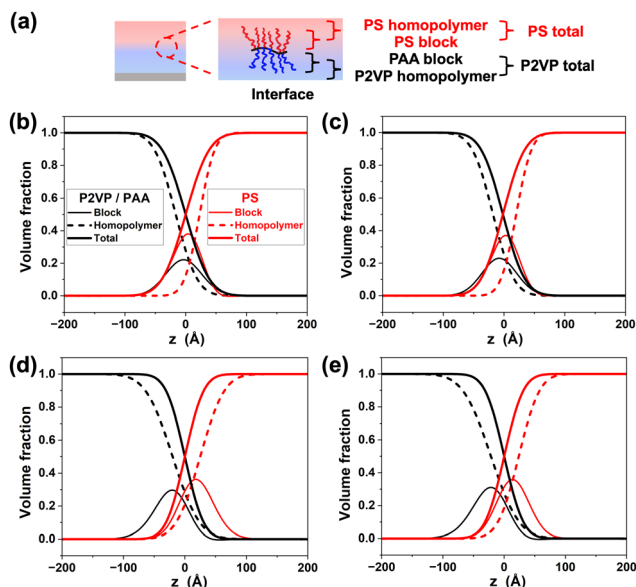
Fig. 3 (a) Schematic illustration of a JBCP at polymer–polymer interface. Volume fraction profiles of different components at interfaces for JBCPs with variation of N_{BB}, (b) N_{BB} = 6, (c) N_{BB} = 24, (d) N_{BB} = 100, and (e) N_{BB} = 250. Z is the distance in Angstrom from the homopolymer interface. The legends for (c)–(e) are same as (b).
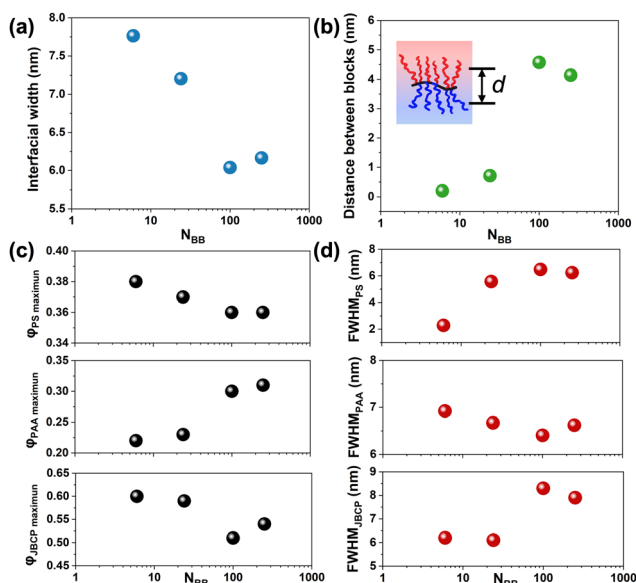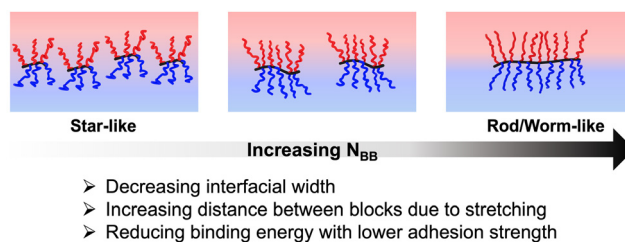

Fig. 4 Characteristics of segment density distributions of JBCPs for different N_{BB}. (a) Interfacial width, derived by solving PS total segments (PS blocks and homopolymers) and P2VP total segments (PAA blocks and P2VP homopolymers) from PS||(DPS-PAA)$_n$||DP2VP||Si. (b) Distance (d) between two blocks obtained by differences between two blocks position using $z = \int_{-\infty}^{\infty} z \mathrm{d}\Phi_{block} / \int_{-\infty}^{\infty} \mathrm{d}\Phi_{block}$, (c) Volume fraction maximum ($\phi_{maximum}$) of PS block, PAA block and JBCP molecule. (d) Full-width half maximum (FWHM) of PS block, PAA block and JBCP molecule.

volume fraction maximum ($\phi_{PAA\,maximum}$) increases (Fig. 4c). This is further supported by inverse trends in the full-width half maximum (FHWM) of the blocks, where FWHM$_{PS}$ increases

Scheme 2 Schematic illustration of interfacial conformation of JBCP compatibilizers with variable N_{BB}.

and FWHM$_{PAA}$ decreases at higher N_{BB} (Fig. 4d). These findings indicate a broader distribution of the PS block at the interface for higher N_{BB} due to the stretching effect. While the PAA block also experiences stretching at elevated N_{BB}, its interaction with P2VP homopolymer ($\chi < 0$) is more pronounced at lower N_{BB}, potentially leading to a broader distribution of the PAA block in the P2VP homopolymer.[51] The combined volume fraction of $\phi_{PAA\,block}$ and $\phi_{PS\,block}$ provides the distribution of the JBCP (ϕ_{JBCP}). It is seen that $\phi_{JBCP\,maximum}$ decreases and FWHM$_{JBCP}$ increases for larger N_{BB}, suggesting that the entire molecule, on average, undergoes a stretching, normal to backbone at higher N_{BB}.

Fig. 5 shows the segmental density distribution for varying GD at N_{BB} = 100. The interfacial width derived from the segmental density distribution aligns with the direct measurements of interfacial width from DPS||(DPS-PAA)$_n$||P2VP contrast (Fig. 6a). As shown in Fig. 6b, d (distance between blocks) exhibits a trend with GD. For GD of 100%, d is 4.6 nm, which slightly increases to 4.7 nm at 80% and peaks at 5.1 nm for 50%. However, a further reduction in GD to 20% results in a decrease of d to 3.2 nm. This behavior can be attributed to the pronounced stretching of PS block and PAA block at large N_{BB}: As GD decreases within a certain range, the backbone likely adopts zig-zag configuration due to the tension exerted by the stretching of the two blocks, leading to an increase in d (Scheme 3). Yet, a more significant reduction in GD resulting in a looser packing of the blocks, diminishing the steric hinderance from neighboring chains (Scheme 3). Consequently, a minimum value of d is observed at GD of 20%. Furthermore, as shown in Fig. 6c and d, the GD of 80% exhibits the lowest $\phi_{PS\,maximum}$, $\phi_{PAA\,maximum}$ and $\phi_{JBCP\,maximum}$ and highest FWHM$_{PS}$, FHWM$_{PAA}$ and FWHM$_{JBCP}$. This suggests that both the blocks and entire molecule have the broadest distribution normal to the interface at GD of 80%, which is consistent with the results of the interfacial widths.

Compatibilization efficiency

The compatibilization efficiency was investigated using the morphology of the thin film blends of PS homopolymer and P2VP homopolymer with added JBCPs.[37] Thin films of the mixture were prepared by spin-coating from tetrahydrofuran (THF), followed by thermal annealing. Ethanol was used to remove the P2VP domains. As seen in Fig. 7a–d, both N_{BB} = 6 and N_{BB} = 24 resulted in a bicontinuous morphology, with a
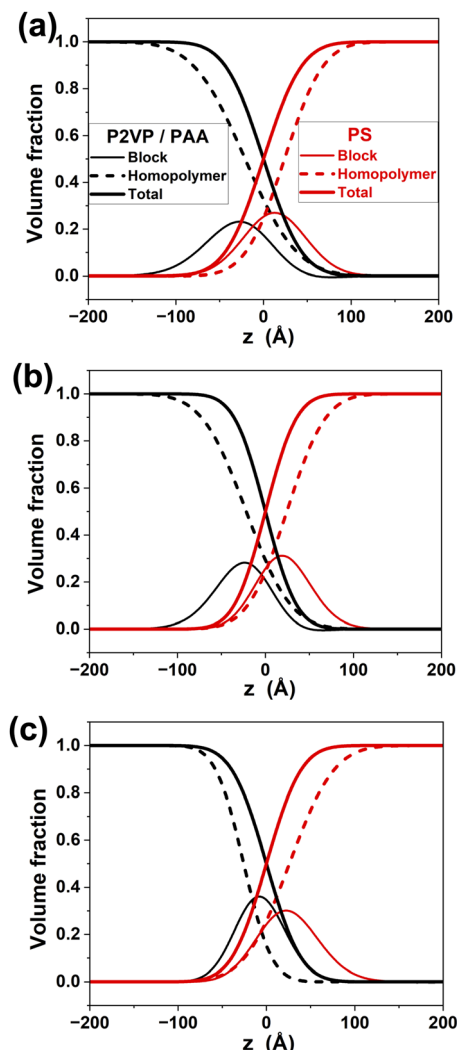
Fig. 5 Volume fraction profiles of different components at interfaces for JBCPs with N_{BB} = 100 at different grafting densities of (a) 80%, (b) 50%, and (c) 20%. Z is the distance from the homopolymer interface. The legends for (b) and (c) are same as (a).
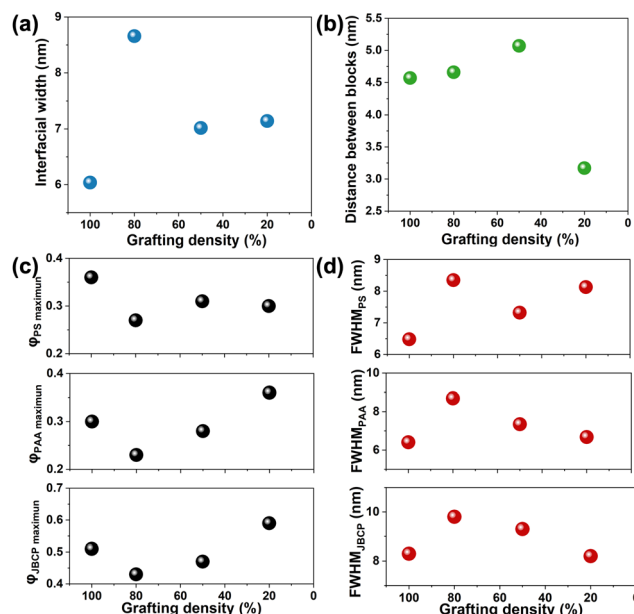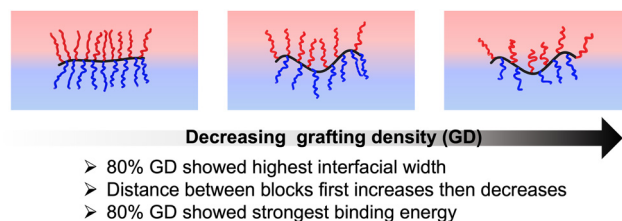

Fig. 6 Characteristics of segment density distributions for different grafting densities (GD) with N_{BB} = 100. (a) Interfacial width solved from PS||(DPS-PAA)$_n$||DP2VP||Si. (b) Distance (d) between two blocks (c) volume fraction maximum ($\phi_{maximum}$) of PS block, PAA block and JBCP molecule. (d) Full-width half maximum (FWHM) of PS block, PAA block and JBCP molecule.

Scheme 3 Schematic illustration of interfacial conformation of JBCP compatibilizers with variable grafting densities for N_{BB} = 100.

characteristic length of 19 μm (determined from Fig. S27, ESI†). For N_{BB} = 100, separated PS domains were dispersed throughout the P2VP matrix (Fig. 7e and f). This pattern was reversed for N_{BB} = 250 (Fig. 7g and h). A bicontinuous morphology is produced by kinetically arresting the phase separation of PS and P2VP, where only JBCPs with sufficiently high binding energy can trap the non-equilibrium morphology (Fig. 7i).[38] We also characterized the thin film morphology using scanning electron miscropy (SEM), which showed same structural information as AFM (Fig. S28, ESI†).

At a GD of 80%, block crowding is reduced. This increases the flexibility of blocks, enhancing interaction between the blocks and the homopolymer, leading to a higher binding energy. As a result, the bicontinuous morphology was observed at GD of 80% (Fig. 8a to b), with a characteristic length of 16 μm (Fig. S26, ESI†). However, as GD is further decreased to 50%, both larger (∼60 μm) and smaller P2VP domains (∼3 μm) are

seen in a PS matrix. At an even lower GD of 20%, only large P2VP domains (∼50 μm) are seen (Fig. 8e and f). These morphologies suggest that, for rod-like JBCPs with a low GD, even though the interactions between the blocks and homopolymer are enhanced, the effective number of side chains per molecule is insufficient to arrest the phase separation. Interestingly, despite the relatively low binding energy at low GD (50% or 20%) of N_{BB} = 100, we noted that P2VP domains appeared to be squeezed between each other without coarsening. This observation indicates that the mechanical strength of interlayer JBCP film is robust enough to prevent domain coarsening at scale of ∼50 μm.

Adhesion strength

Introducing JBCPs to the interface can increase the adhesion between two immiscible homopolymers. This adhesion
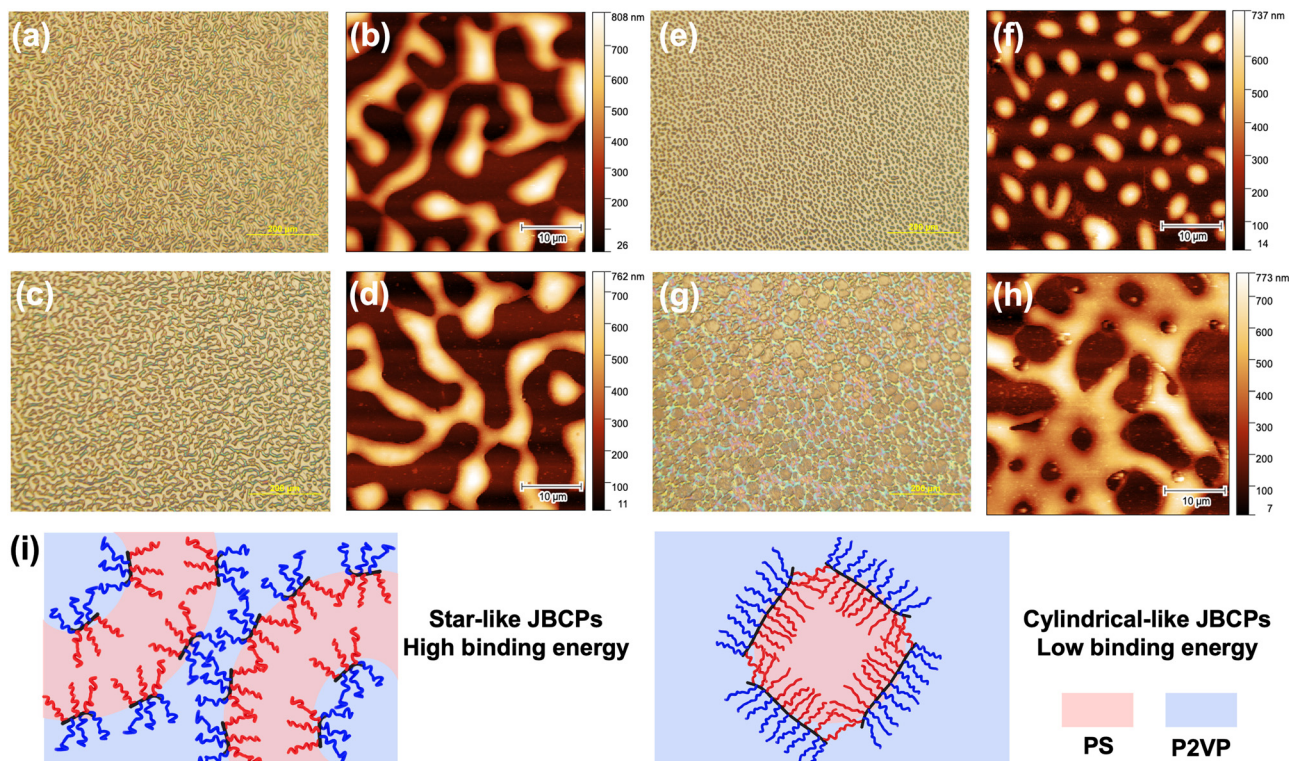
Fig. 7 Morphologies of thin film blends contained PS homopolymer and P2VP homopolymer (70 wt% to 30 wt%) with 10 wt% JBCP additives of different N_{BB}. GD = 100% for all N_{BB}. POM images of (a) N_{BB} = 6, (c) N_{BB} = 24, (e) N_{BB} = 100, and (g) N_{BB} = 250. AFM images of (b) N_{BB} = 6, (d) N_{BB} = 24, (f) N_{BB} = 100, and (h) N_{BB} = 250. (i) Schematic illustration of N_{BB} effect on binding energy at homopolymer interfaces. P2VP domain was washed by ethanol after thermal annealing of thin film blends.
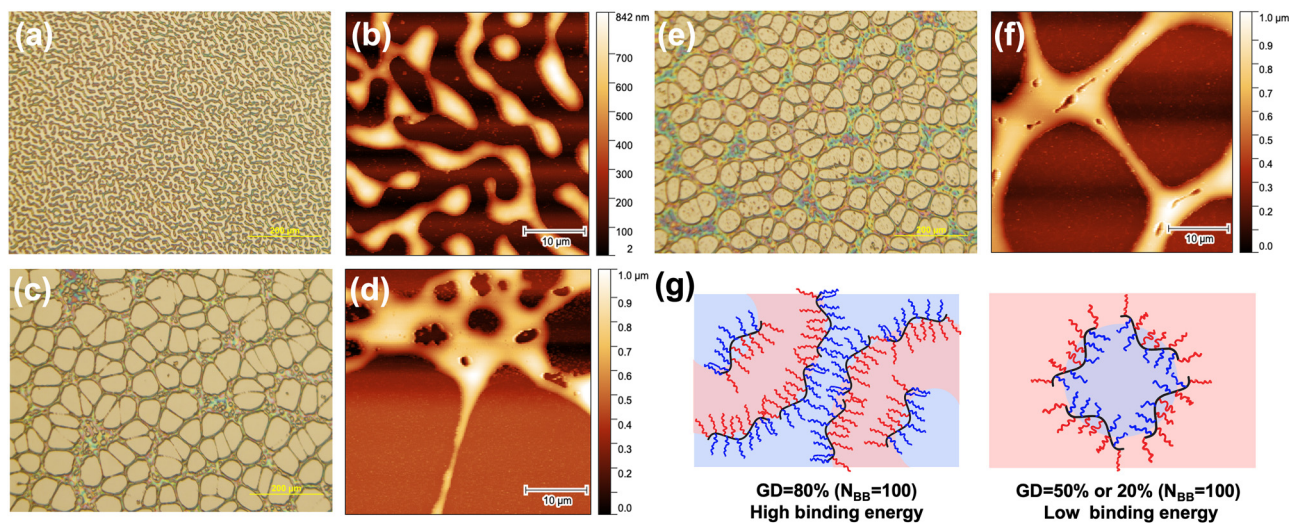

Fig. 8 Morphologies of thin film blends containing PS homopolymer and P2VP homopolymer (70 wt% to 30 wt%) with 10 wt% JBCP for different grafting densities at N_{BB} = 100. POM images of grafting density (a) 80%, (c) 50%, and (e) 20%. AFM images of (b) 80%, (d) 50%, and (f) 20%. (g) Schematic illustration of grafting density effect on binding energy at homopolymer interfaces. P2VP domain was washed by ethanol after thermal annealing of thin film blends.

strength is critical for improving stress transfer between the components, especially when JBCPS are utilized as compatibilizer for polymer upcycling. We employed the asymmetric double cantilever beam (ADCB) test, a method commonly used for glassy materials, to assess the adhesion strength when the JBCPs are directly placed at the homopolymer interfaces
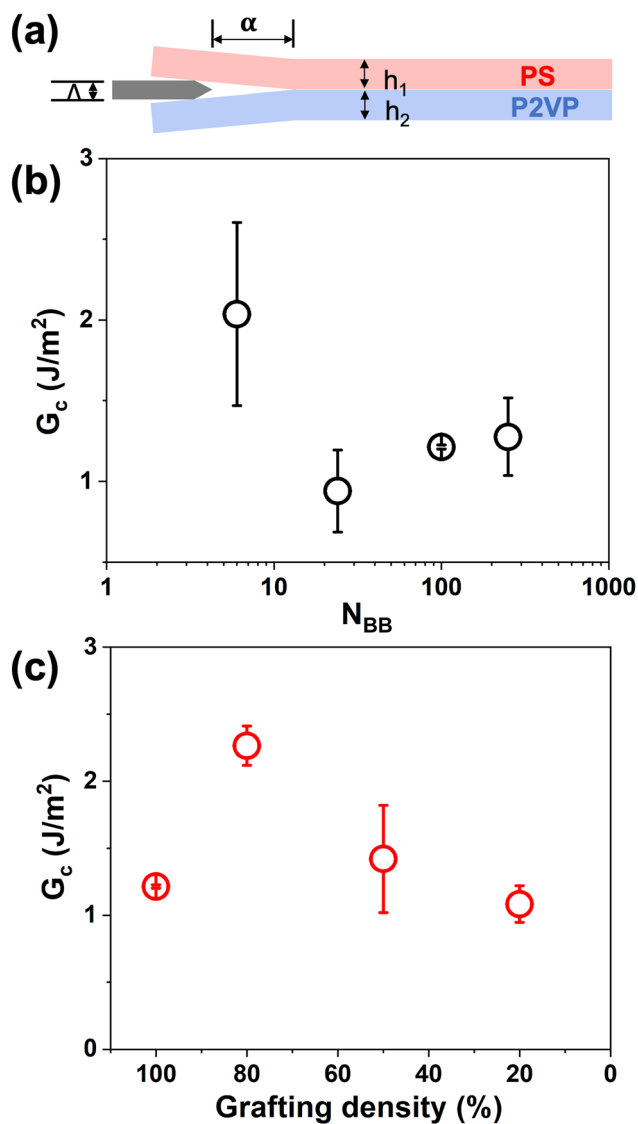
Fig. 9 Adhesion strength of JBCPs at homopolymer interface measured by asymmetric double cantilever beam (ADCB) test. (a) Scheme of ADCB test. Critical energy release rate (G_C) as a function of (b) N_{BB} (grafting density = 100%) and (c) grafting density (N_{BB} = 100%).

(Fig. 9a). The critical energy release rate is given by

$$G_C = \frac{3\Delta_{razor}^2 E_1 h_1^3 E_2 h_2^3}{8\alpha^4} \left[\frac{E_1 h_1^3 C_2^2 + E_2 h_2^3 C_1^2}{(E_1 h_1^3 C_2^3 + E_2 h_2^3 C_1^3)^2} \right],$$

where

$$C_1 = 1 + 0.64\frac{h_1}{\alpha}, \ C_2 = 1 + 0.64\frac{h_2}{\alpha},$$

subscript 1 and 2 are PS and P2VP, respectively, E is Young's modulus, h is the thickness of the beam, α is the crack length (distance from the razor blade tip to the crack tip, which is measured after insertion of the razor blade overnight), and Δ_{razor} is the thickness of the razor blade.[36] For different architectures, $a \sim 5$ nm JBCP layer was placed at interface. As shown in Fig. 9b, the highest G_C value was observed for N_{BB} = 6.

This is consistent with the interfacial width and thin film blend morphology studies. As N_{BB} increases, G_C first decreases at N_{BB} = 24, then shows a slight increase at N_{BB} = 100 and 250. Although the interactions between blocks and homopolymers decrease with increasing N_{BB}, this effect stabilizes rapidly. However, the number of blocks attached to a single molecule continues to increase at higher N_{BB}, contributing to a minor increases of G_C at N_{BB} = 100 and 250. We also evaluated the adhesion strength for different GD of N_{BB} = 100, as shown in Fig. 9c. A slight GD reduction (80%) resulted in the highest G_C. Further GD reduction led to decrease in G_C. It is worth noting that the N_{SC} for PS is 21 and 32 for PAA. Both are significantly below the entanglement molecular weight (M_e) of PS ($\sim$150 repeat units) and P2VP ($\sim$150 repeat units) homopolymers.[36] This explains the relatively low G_C values in this study, compared to previous studies where the molecular weight of linear BCPs significantly exceeded M_e. Nonetheless, these results underscore the potential BCP architecture in enhancing binding energy per molecule and improving adhesion strength.

Conclusions

In summary, we studied the behavior of Janus bottlebrush copolymers (JBCPs) at the interface between two immiscible homopolymers using neutron reflectivity (NR). We varied both the backbone length (N_{BB}) and grafting density (GD) to understand the influence of architecture. We linked their interfacial behavior to the compatibilization efficiency, where the compatibilization efficiency is defined as the efficiency to reduce interfacial tension and increase the adhesion between immiscible domains. We investigated the morphology of thin film blends containing both homopolymers and JBCPs and the adhesion strength was further assessed from the critical energy release rate (G_C) using asymmetric double cantilever (ADCB) test. Our findings showed that the smallest N_{BB} (N_{BB} = 6) achieved the maximum interfacial width. Using NR, the segmental density distribution of all the components across the interface were evaluated. As N_{BB} increased, the distance between blocks increased due to the stretching, which diminishes the interaction between blocks and homopolymers. This led to a reduced interfacial width. The morphology of the thin film blends further showed that a lower N_{BB} can arrest the phase separation, producing a bicontinuous structure. ADCB test results also showed that smallest N_{BB} had the strongest adhesion. For higher N_{BB} (specifically N_{BB} = 100), a modest reduction in GD enhances the interaction between the blocks and homopolymers by increasing the flexibility of blocks, while maintained a relatively high number of blocks per molecule. However, further reducing GD causes the number of blocks to decrease, leading to a poorer compatibilization efficiency. Consequently, the interfacial width is greatest at 80% GD for N_{BB} = 100, then decreases. Notably, only the 80% GD produced a bicontinuous morphology in thin film blends and showed the highest adhesion strength in ADCB test. In conclusion, our findings offer valuable insights into designing JBCP architectures

as efficient compatibilizers, paving the way for innovating new BCP compatibilizers for polymer upcycling.

Author contributions

T. E. and T. P. R. conceptualized this research. Z. C. performed sample preparation, NR, AFM and ADCB experiments. H. S. synthesized JBCPs polymer. M. H. assisted NR experiments. X. G. assisted data analysis. A. E. R. assisted SEM experiments. J. J. assisted GPC measurements. H. W. assisted NR experiments. M. D. assisted off-specular neutron reflection data analysis. Z. C. and H. S. wrote original manuscript. All authors revised the manuscript. All authors have given approval to the final version of the manuscript.

Conflicts of interest

There are no conflicts to declare.

Acknowledgements

Notes and references

1 D. Kwon, *Nature*, 2023, **616**, 234–237.
2 L. T. J. Korley, T. H. Epps, 3rd, B. A. Helms and A. J. Ryan, *Science*, 2021, **373**, 66–69.
3 J. Maris, S. Bourdon, J.-M. Brossard, L. Cauret, L. Fontaine and V. Montembault, *Polym. Degrad. Stab.*, 2018, **147**, 245–266.
4 Z. O. G. Schyns and M. P. Shaver, *Macromol. Rapid Commun.*, 2021, **42**, e2000415.
5 J. L. Self, A. J. Zervoudakis, X. Peng, W. R. Lenart, C. W. Macosko and C. J. Ellison, *JACS Au*, 2022, **2**, 310–321.
6 T. P. Russell, *Curr. Opin. Colloid Interface Sci.*, 1996, **1**, 107–115.
7 J. M. Eagan, J. Xu, R. Di Girolamo, C. M. Thurber, C. W. Macosko, A. M. LaPointe, F. S. Bates and G. W. Coates, *Science*, 2017, **355**, 814–816.
8 K. Klimovica, S. Pan, T. W. Lin, X. Peng, C. J. Ellison, A. M. LaPointe, F. S. Bates and G. W. Coates, *ACS Macro Lett.*, 2020, **9**, 1161–1166.
9 T. Zhou, D. Qiu, Z. Wu, S. A. N. Alberti, S. Bag, J. Schneider, J. Meyer, J. A. Gámez, M. Gieler, M. Reithmeier, A. Seidel and F. Müller-Plathe, *Macromolecules*, 2022, **55**, 7893–7907.
10 C. R. López-Barrón and A. H. Tsou, *Macromolecules*, 2017, **50**, 2986–2995.
11 Z. Li, M. Tang, S. Liang, M. Zhang, G. M. Biesold, Y. He, S.-M. Hao, W. Choi, Y. Liu, J. Peng and Z. Lin, *Prog. Polym. Sci.*, 2021, **116**.
12 J. M. Ren, T. G. McKenzie, Q. Fu, E. H. Wong, J. Xu, Z. An, S. Shanmugam, T. P. Davis, C. Boyer and G. G. Qiao, *Chem. Rev.*, 2016, **116**, 6743–6836.
13 T. P. Russell, S. H. Anastasiadis, A. Menelle, G. P. Felcher and S. K. Satija, *Macromolecules*, 2002, **24**, 1575–1582.
14 Z. Chen, C. Steinmetz, M. Hu, E. B. Coughlin, H. Wang, W. T. Heller, W. Bras and T. P. Russell, *Macromolecules*, 2023, **56**, 8308–8322.
15 T. P. Russell, A. M. Mayes, V. R. Deline and T. C. Chung, *Macromolecules*, 2002, **25**, 5783–5789.
16 K. Miyagi, H. Mei, T. Terlier, G. E. Stein and R. Verduzco, *Macromolecules*, 2020, **53**, 6720–6730.
17 P. F. Green and T. P. Russell, *Macromolecules*, 2002, **24**, 2931–2935.
18 K. R. Shull, E. J. Kramer, G. Hadziioannou and W. Tang, *Macromolecules*, 2002, **23**, 4780–4787.
19 C. A. Dai, B. J. Dair, K. H. Dai, C. K. Ober, E. J. Kramer, C. Y. Hui and L. W. Jelinski, *Phys. Rev. Lett.*, 1994, **73**, 2472–2475.
20 J. Y. Carrillo, Z. Chen, U. I. Premadasa, C. Steinmetz, E. B. Coughlin, B. Doughty, T. P. Russell and B. G. Sumpter, *Nanoscale*, 2023, **15**, 1042–1052.
21 Z. Chen, A. E. Ribbe, C. Steinmetz, E. B. Coughlin, M. Hu, X. Gan and T. P. Russell, *Angew. Chem., Int. Ed.*, 2024, e202400127.
22 L. Elias, F. Fenouillot, J. C. Majesté, P. Alcouffe and P. Cassagnau, *Polymer*, 2008, **49**, 4378–4385.
23 M. Seyedi, M. Savchak, A. Tiiara and I. Luzinov, *ACS Appl. Mater. Interfaces*, 2022, **14**, 35074–35086.
24 M. Zhang, C. Jiang, Q. Wu, G. Zhang, F. Liang and Z. Yang, *ACS Macro Lett.*, 2022, **11**, 657–662.
25 H. He and F. Liang, *Chem. Mater.*, 2022, **34**, 3806–3818.
26 H.-L. He and F.-X. Liang, *Chinese J. Poly. Sci.*, 2023, **41**, 500–515.
27 H. G. Seong, Z. Chen, T. Emrick and T. P. Russell, *Angew. Chem., Int. Ed.*, 2022, **61**, e202200530.
28 G. Xie, M. R. Martinez, M. Olszewski, S. S. Sheiko and K. Matyjaszewski, *Biomacromolecules*, 2019, **20**, 27–54.
29 K. H. Kim, M. Kim, J. Moon, J. Huh and J. Bang, *ACS Macro Lett.*, 2021, **10**, 346–353.
30 R. Verduzco, X. Li, S. L. Pesek and G. E. Stein, *Chem. Soc. Rev.*, 2015, **44**, 2405–2420.
31 H. G. Seong, Z. Fink, Z. Chen, T. Emrick and T. P. Russell, *ACS Nano*, 2023, **17**, 14731–14741.
32 K. H. Dai, L. J. Norton and E. J. Kramer, *Macromolecules*, 2002, **27**, 1949–1956.
33 T. P. Russell, A. Menelle, W. A. Hamilton, G. S. Smith, S. K. Satija and C. F. Majkrzak, *Macromolecules*, 2002, **24**, 5721–5726.
34 S. Dutta, M. A. Wade, D. J. Walsh, D. Guironnet, S. A. Rogers and C. E. Sing, *Soft Matter*, 2019, **15**, 2928–2941.
35 A. E. Levi, J. Lequieu, J. D. Horne, M. W. Bates, J. M. Ren, K. T. Delaney, G. H. Fredrickson and C. M. Bates, *Macromolecules*, 2019, **52**, 1794–1802.
36 C. Creton, E. J. Kramer, C. Y. Hui and H. R. Brown, *Macromolecules*, 2002, **25**, 3075–3088.
37 A. H. Mah, P. Afzali, L. Qi, S. Pesek, R. Verduzco and G. E. Stein, *Macromolecules*, 2018, **51**, 5665–5675.

38 K. C. Bryson, T. I. Löbling, A. H. E. Müller, T. P. Russell and R. C. Hayward, *Macromolecules*, 2015, **48**, 4220–4227.

39 H.-F. Fei, B. M. Yavitt, S. Nuguri, Y.-G. Yu and J. J. Watkins, *Macromolecules*, 2021, **54**, 10943–10950.

40 M. Hu, X. Li, J. Rzayev and T. P. Russell, *Macromolecules*, 2021, **54**, 11449–11458.

41 M. Hu, X. Gan, Z. Chen, H. G. Seong, T. Emrick and T. P. Russell, *J. Polym. Sci.*, 2023, DOI: **10.1002/pol.20230530**.

42 J. Y. Kelly, J. N. L. Albert, J. A. Howarter, C. M. Stafford, T. H. Epps and M. J. Fasolka, *J. Polym. Sci., Part B: Polym. Phys.*, 2012, **50**, 263–271.

43 D. M. Yu, D. M. Smith, H. Kim, J. Rzayev and T. P. Russell, *Macromolecules*, 2019, **52**, 6458–6466.

44 T. P. Russell, *Mater. Sci. Rep.*, 1990, **5**, 171–271.

45 K. H. Dai, E. J. Kramer and K. R. Shull, *Macromolecules*, 2002, **25**, 220–225.

46 C. Creton, E. J. Kramer and G. Hadziioannou, *Macromolecules*, 2002, **24**, 1846–1853.

47 T. Hashimoto, S. Koizumi and H. Hasegewa, *Phys. B*, 1995, **213–214**, 676–681.

48 Y. Mai and A. Eisenberg, *Chem. Soc. Rev.*, 2012, **41**, 5969–5985.

49 A. Boker, J. He, T. Emrick and T. P. Russell, *Soft Matter*, 2007, **3**, 1231–1248.

50 M. Hu, X. Li, W. T. Heller, W. Bras, J. Rzayev and T. P. Russell, *Macromolecules*, 2023, **56**, 2418–2428.

51 J. G. Kennemur, *Macromolecules*, 2019, **52**, 1354–1370.